Organic carbon, sea level and carbonate weathering controls on marine carbon isotope perturbations across the Hirnantian glaciation

Jiaqiang Zhang [a,b,c,d], Zhen Qiu [a,b,*], Wenjiao Xiao [c,e,*], Paul B. Wignall [d], Weiliang Kong [b], Benjamin J. W. Mills [d], Yijun Xiong [d], Simon W. Poulton [d]

[a]*School of Geoscience and Technology, Southwest Petroleum University, Chengdu, 610500, China*

[b]*Research Institute of Petroleum Exploration & Development, China National Petroleum Corporation, Beijing, China*.

[c]*State Key Laboratory of Lithospheric and Environmental Coevolution, Institute of Geology and Geophysics, Chinese Academy of Sciences, Beijing 100029, China*

[d]*School of Earth and Environment, University of Leeds, Leeds LS2 9JT, UK*

[e]*Xinjiang Research Center for Mineral Resources, Xinjiang Institute of Ecology and Geography, Chinese Academy of Sciences, Urumqi 830011, China*

*Corresponding author.

E-mail addresses: qiuzhen316@163.com (Z. Qiu), wj-xiao@mail.iggcas.ac.cn (W. Xiao)

Keywords: Hirnantian glaciation, HICE, Dissolved inorganic carbon, Calcium isotopes, Yangtze Shelf

ABSTRACT

The Hirnantian isotopic carbon excursion (HICE) records a dramatic perturbation to the global carbon cycle across the Late Ordovician Hirnantian glaciation (ca. 444.5 million years ago). The HICE is characterized by variable duration and amplitude in global records, but its ultimate driver, and controls on the observed variability, are poorly understood. Here, we present a comprehensive compilation of geochemical data and paired carbon and calcium isotope records for two continuous Hirnantian sections at Wanhe and Shuanghe on the Yangtze Shelf (South China). Our results reveal a lateral gradient of up to 4‰ in organic carbon isotope ($\delta^{13}C_{org}$) values across the shelf, decreasing from nearshore to offshore. Carbonate carbon isotope ($\delta^{13}C_{carb}$) data from the Wanhe and Shuanghe sections also show pronounced variability, which cannot be fully explained by primary mineralogical changes or early marine diagenesis. We therefore interpret the spatial $\delta^{13}C_{org}$ patterns as reflecting, at least in part, shelf-scale heterogeneity in seawater dissolved inorganic carbon isotope ($\delta^{13}C_{DIC}$) values. Our compilation further suggests that substantial organic carbon burial likely triggered the HICE, while sea-level change subsequently drove the asynchronous, spatially heterogeneous changes in seawater $\delta^{13}C_{DIC}$ values. Additionally, enhanced carbonate weathering, linked to falling syn-glacial sea-level, amplified the spatial heterogeneity in regional marine $\delta^{13}C_{DIC}$ values. Moderate $\delta^{13}C_{org}$ changes (<+2‰) are observed in central shelf areas across the Hirnantian glaciation, suggesting that the global carbon cycle perturbations during this ice age were of more

modest amplitude than often suggested.

1. Introduction

The Late Ordovician is marked by the first of the “Big Five” mass extinctions (Harper, 2023), which coincided with substantial continental glaciation (the Hirnantian glaciation; Finnegan et al., 2011). A marked fall in atmospheric CO_2 levels is proposed to have occurred during this glacial period (e.g., Pohl et al., 2016; Zhang et al., 2024), coincident with a global positive carbon isotope ($\delta^{13}C$) excursion (the Hirnantian isotopic carbon excursion; HICE). The HICE began in the latest Katian (ca. 445.2 million years ago), with variable amplitudes ranging from +1‰ to over +6‰ across different sections (Melchin and Holmden, 2006; Fig. 1A-B). Marine anoxia and increased primary productivity were reportedly widespread in late Katian oceans (Hammarlund et al., 2012; Zou et al., 2018; Dahl et al., 2021; Qiu et al., 2022b; Liang et al., 2024), and thus elevated organic carbon burial has been invoked as a main driver for the HICE (e.g., Brenchley et al., 1994; Zhang et al., 2024). However, this hypothesis appears to be inconsistent with an apparent decrease in total organic carbon (TOC) content in both deep marine (Fig. 1C) and shelf (Fig. 1D) settings at the peak of the HICE (e.g., Melchin and Holmden, 2006; Yang and Fan, 2025).

Although post-depositional diagenetic alteration could potentially cause varying degrees of change in carbonate carbon isotope ($\delta^{13}C_{carb}$) compositions (e.g., Crockford et al., 2020; Jones et al., 2020; Adiatma et al., 2024), this process does not

provide a robust explanation for the observed heterogeneity in organic carbon isotope ($\delta^{13}C_{org}$) records, as diagenetic alteration has limited effects on $\delta^{13}C_{org}$ values in sedimentary rocks (e.g., Jiang et al., 2012). Instead, Kump et al. (1999) proposed that the HICE may have resulted from syn-glacial weathering of carbonate platforms and associated increases in ^{13}C input to the ocean. However, this model appears to require unrealistic increases in the weathering influx to fully account for a $\delta^{13}C$ shift of up to +6‰ in the global ocean (Melchin and Holmden, 2006). Alternatively, Sánchez-Roda et al. (2024) suggested that the positive shift could reflect a decline in carbonate burial during the glacial episode, but as with other models, this would not explain the spatially heterogeneous and asynchronous nature of the HICE.

Variability in the amplitude and duration of the HICE may document spatial heterogeneity in marine dissolved inorganic carbon isotopic ($\delta^{13}C_{DIC}$) compositions (Melchin and Holmden, 2006; LaPorte et al., 2009; Ahm et al., 2017). While recent work has revealed the presence of marine DIC depth gradients during the Hirnantian glaciation (Yang et al., 2024), the exact spatial pattern of marine $\delta^{13}C_{DIC}$ variations on a regional scale remains poorly defined. To address this, we initially provide a series of reconstructions of spatiotemporal trends in marine $\delta^{13}C_{DIC}$ values by mapping $\delta^{13}C_{org}$ data from 43 sites across the Yangtze Shelf. Paired $\delta^{13}C_{org}$, $\delta^{13}C_{carb}$ and carbonate calcium isotope ($\delta^{44}Ca$) data from two continuous sections at Wanhe and Shuanghe then allow a detailed evaluation of the roles of sea level change and carbonate weathering on marine C and Ca cycling. Our integrated analyses provide new insight

into early Paleozoic C isotope dynamics in the ocean, and provide a compelling explanation for the controversial variability of HICE records.

2. Geological setting

South China was situated at a low latitude during the Ordovician– Silurian transition (Cocks and Torsvik, 2021; Fig. 2A), and consisted of the Yangtze Block to the northwest and the Cathaysia Block to the southeast (Lin et al., 2024). During the Ordovician– Silurian transition, the northern region of the tropical South China Block was flooded by the epicontinental Yangtze Shelf Sea, which deepened toward the north and passed into the Panthalassa Ocean (Fig. 2B). Upper Ordovician strata in the Yangtze region comprise the early–mid Katian Pagoda and mid–late Katian Linhsiang platform limestones. The Linhsiang Formation is overlain by late Katian to earliest Hirnantian strata, including carbonaceous shales of the Wufeng Formation in deep-water shelf areas, and argillaceous limestones interbedded with calcareous shales of the Daduhe Formation in shallow-water proximal shelf areas. These two coeval units generally record regional sea-level rise (Fig. 1F) and increased terrestrial inputs due to the northward progression of the Kwangsian Orogeny (Chen et al., 2014). The Hirnantian Kuanyinchiao Bed, consisting of calcareous mudstones with carbonate concretions and abundant shelly fossils of the cool-water *Hirnantia* fauna, accumulated during a glacial maximum (Rong et al., 2020). The succeeding graptolitic shales of the Lungmachi Formation were deposited during post-glacial marine transgression and ocean euxinia from the latest Hirnantian to Rhuddanian (Zou et al.,

105 2018). In the Yichang and Central Guizhou uplifts, the Lungmachi Shale directly
106 overlies the Linhsiang limestones, reflecting a Late Ordovician to early Silurian
107 depositional hiatus, with local exposure and erosion of the Late Ordovician carbonates
108 (i.e., Pagoda and Linhsiang formations) during the maximum extent of the Hirnantian
109 glaciation (Chen et al., 2018).

110 In this study, we obtained samples from the Wanhe (103.4762°E, 27.7552°N) and
111 Shuanghe (104.8842°E, 28.3847°N) sections on the Yangtze Shelf (Fig. 2B). During the
112 Late Ordovician, the Wanhe section was situated in a nearshore shallow-water setting
113 characterized by limestone deposition. By contrast, the Shuanghe section was
114 consistently situated in a moderately deep mid-shelf setting, dominated by shale
115 deposition. However, much of the shale at Shuanghe is calcareous, with an average
116 carbonate content of 37.4 wt% (Qiu et al., 2022a). The carbonate minerals primarily
117 comprise calcite and dolomite, and occur as silty carbonate laminae, dispersed grains
118 within the fine-grained matrix, or calcareous fossils (Qiu et al., 2022; Wu et al., 2022).
119 The sedimentary characteristics and biostratigraphy of the two sections can be
120 correlated with the Wangjiawan section, representing the Global Boundary
121 Stratigraphic Section and Point (GSSP) for the base of the Hirnantian Stage (Chen et
122 al., 2006).

123 **3. Materials and methods**

124 A total of 151 samples were collected from the Wanhe (108) and Shuanghe (43)
125 sections. Before geochemical analysis, the fresh samples were carefully trimmed to

remove weathered surfaces, visible veins and pyrite nodules. The remaining sample was then powdered to approximately 200 mesh using an agate mill. All samples from the Wanhe section were analyzed for major elements, TOC content and organic carbon isotopes at the Key Laboratory of Petroleum Resources of the Northwest Institute of Eco-Environment and Resources, Chinese Academy of Sciences. Additionally, 84 samples from the Wanhe (41) and Shuanghe (43) sections were analyzed for carbonate carbon isotopes, Ca isotopes and trace element contents in carbonate minerals at the State Key Laboratory of Geological Processes and Mineral Resources, China University of Geosciences, Wuhan, China. All data are shown in Table S1. We also compiled Ca/Al, calcite, TOC, and carbon isotope data from 13 globally-distributed locations (Fig. S1; Table S2), and 49 cores and sections from South China (Fig. S2; Table S3).

3.1 Geochemical analyses

3.1.1 Organic carbon contents and isotopes

Prior to analysis, ~2 g of dried sample powder was decarbonated via two sequential dissolutions with 4 M HCl at room temperature. Samples were then washed with deionized water to remove all remaining acid and dried at 50℃. TOC content was measured using a CS-902C High Frequency Infrared C-S analyzer. The analytical reproducibility was better than ±0.1% based on duplicate analyses. Organic carbon isotopes ($\delta^{13}C_{org}$) were analyzed using a Finnigan MAT253 Mass Spectrometer and reported in standard δ-notation relative to the Vienna Pee Dee Belemnite (VPDB)

standard. The analytical reproducibility of $\delta^{13}C_{org}$ was better than ±0.1‰.

3.1.2 Carbonate carbon isotope analysis

About 100 mg of sample powder was weighed into a 10 mL Na glass vial, and then sealed by a butyl rubber septum. After flushing with helium gas, the sample was reacted with 100% phosphoric acid at 72°C to release CO_2. The carbonate carbon isotope ($\delta^{13}C_{carb}$) compositions of the released CO_2 were then measured with a MAT253 Mass Spectrometer, and isotope data were calculated relative to the VPDB standard. The analytical reproducibility was better than ±0.1‰.

3.1.3 Elemental analyses

For bulk major element analysis, ~4 g of dried sample powder was weighed into a mold with boric acid lining the edges and bottom. The powdered samples were pressed into a pellet with an inner diameter of 32 mm using a ZHY-401A press machine at a pressure of 30 tons. Bulk major element analyses were measured using a PANalytical Sequential X-ray Fluorescence (XRF) spectrometer. The analytical precision for all major elements was maintained at better than ±3%.

For bulk trace element analysis, ~50 mg of sample powder was weighed into Teflon beakers. Sequentially, 1.5 mL of 68% HNO_3, 1.5 mL of HF, and 0.01 mL of $HClO_4$ were added. Afterwards, the Teflon beakers were placed on a hotplate at 140°C. Dissolved samples were evaporated to dryness, then re-dissolved in 1.50 mL HNO_3 and 1.50 mL HF. Then the capped Teflon beakers were placed into an oven at 195°C for over 48 h. Dissolved samples were evaporated to dryness, and then 3 mL of HNO_3

was added. Re-dissolved samples were evaporated to dryness, and then 3 mL of 50% HNO_3 was added and the beakers placed into an oven at 150°C for 24 h. The dissolved samples were transferred into 100 mL tubes, and Rh internal standard solution was added. Deionized water was added into the tube to 100 g, ensuring the concentration of Rh in the solution was 50 mg/mL. The final solutions were analyzed using an inductively coupled plasma mass spectrometer (ICP-MS Agilent 7700e).

For the analysis of trace elements in carbonates, ~200 mg of sample powder was individually weighed into centrifuge tubes, and 2 mL of deionized water was added. After 10 mins vibration, the samples were centrifuged and then all supernatant was removed. The deionized water washing procedure was repeated. After washing, the samples were dried and finely re-ground. Next, ~50 mg of the dried sample powder was weighed into a new centrifuge tube, and 0.25 mL of acetic acid (0.86 M) was added. The samples were sonicated for 30 minutes, then allowed to react at room temperature for 24 h (first acidification). After centrifugation, the supernatant was discarded. To ensure complete removal of absorbed Ca, this acetic acid washing procedure was performed again. After the second acidification, the samples were dried and re-ground. Subsequently, the samples were re-dissolved with 0.5 mL of 0.86 M acetic acid. After 30 minutes vibration, the samples were allowed to react at room temperature for 24 h (third acidification). After centrifugation, the supernatant was carefully transferred into a clean Teflon vial. This acid extraction step was repeated (fourth acidification), and the resulting supernatant was added to the same Teflon vial.

The combined solution was then analyzed for trace elements using an ICP-MS (Agilent 7700e).

3.1.4 Calcium isotope analysis of carbonate minerals

In this study, we analyzed the Ca isotope compositions of carbonate minerals, rather than whole-rock samples. The same extraction procedure described above for testing trace elements in carbonate minerals was applied, and the final solutions obtained from the combined third and fourth acidification steps were used for Ca isotope measurements. Firstly, an aliquot containing about 40 μg of Ca was transferred into a 7 mL vial. The solution was dried and re-dissolved with 400 mL of 4 mol/L HNO_3 and then loaded on DGA extraction chromatography resin to purify. About 6 mL of 4 mol/L HNO_3 was added to completely rinse off matrix elements. Then, 3 mL of deionized water was added to quantitatively elute the Ca. The purified sample solutions were evaporated to dryness and re-dissolved with 2 mL of 0.35 mol/L HNO_3 prior to calcium isotope measurements. The final sample solutions were measured for calcium isotope ratios using a multi-collector inductively coupled plasma mass spectrometer (MC-ICP-MS; Nu Plasma 1700) operated in high-resolution mode. The Ca isotopic compositions of the samples are reported as δ-notation relative to seawater ($\delta^{44}Ca$–SW):

$$\delta^{44}Ca\ (\text{in}\ ‰) = [(^{44}Ca / {}^{40}Ca)_{sample} / (^{44}Ca / {}^{40}Ca)_{SW} - 1] \times 1000$$

Measurement uncertainty for each sample was ±0.06‰ (two-standard deviation: 2SD), and the long-term external precision of $\delta^{44}Ca$ was better than ±0.07‰ (2SD) (Li et al.,

2018). The average $\delta^{44}Ca$ value of the SRM 915a standard relative to seawater was 1.92 ± 0.07‰.

3.2 Age model

To construct shelf-scale $\delta^{13}C_{DIC}$ variability across the Hirnantian glaciation, we compiled approximately 2100 $\delta^{13}C_{org}$ data points from 43 drill cores and outcrop sections on the Yangtze Shelf (Fig. S2). Each sample and compiled data point was assigned an interpreted age based on age-constrained graptolite zones (Fig. S3). The Stage boundary ages and durations of each graptolite zone are derived from the latest International Chronostratigraphic Chart (v2024/12) and the Geologic Time Scale 2012 (Cooper et al., 2012). Linear ages were constructed assuming a constant sedimentation rate within the age-controlled graptolite zone. To minimize the influence of outliers and age uncertainties, we extracted six $\delta^{13}C_{org}$ values with 1 Ma time span between 447.5 Ma and 442.5 Ma from the 10% LOWESS (locally weighted scatterplot smoothing) fitted $\delta^{13}C_{org}$ profile for each section (Table S3). These extracted $\delta^{13}C_{org}$ values were then used to generate a series of time-slice $\delta^{13}C_{org}$ records using Surfer software. The 1σ uncertainty on the extracted $\delta^{13}C_{org}$ values was<0.5‰. A kriging interpolation method in Surfer was applied for map grids.

4. Results

The $\delta^{13}C_{org}$ and $\delta^{13}C_{carb}$ profiles show considerable variability throughout the Pagoda and Daduhe formations at Wanhe (Fig. 3A). Overall, calcareous shale and

mudstone intervals show lower $\delta^{13}C_{org}$ and $\delta^{13}C_{carb}$ values compared to carbonate-rich intervals. In the early Hirnantian, a positive $\delta^{13}C_{org}$ excursion (i.e., HICE) of +1.8‰ is observed, whereas no clear HICE signal is evident in the $\delta^{13}C_{carb}$ profile. This is followed by relatively stable $\delta^{13}C_{org}$ (average -29.7‰) and $\delta^{13}C_{carb}$ (average -0.58‰) values in the Lungmachi Formation. The $\delta^{13}C_{carb}$ profile for the Shuanghe section fluctuates between -1.34‰ and +1.26‰ (Fig. 3B). Similar to the $\delta^{13}C_{org}$ profile, the $\delta^{13}C_{carb}$ profile exhibits a slight (~1.1‰) Hirnantian positive excursion starting at ~ 7.0 m in the Wufeng Formation. However, distinct $\delta^{13}C_{carb}$ troughs occur when $\delta^{13}C_{org}$ reaches its maximum.

Carbonate $\delta^{44}Ca$ at Wanhe ranges from -1.41‰ to -0.93‰, with variability in the late Katian Daduhe Formation and the Hirnantian Kuanyinchiao Bed (Fig. 3A). This is followed by relatively stable low values that persist into the Silurian. In the Shuanghe section, the carbonate $\delta^{44}Ca$ profile has high values (average -0.99‰) in the basal Linhsiang limestones. This is followed by consistently lower values around -1.38‰, before a rapid increase at the onset of the HICE. Subsequently, carbonate $\delta^{44}Ca$ records decrease to low values with mild fluctuations, reaching a minimum of -1.57‰ within the peak HICE interval. With the exception of the two samples at the top, the Lungmachi Formation shows a nearly invariant carbonate $\delta^{44}Ca$ value of around -1.38‰, similar to pre-HICE values.

5. Discussion

5.1 Shelf-scale $\delta^{13}C_{org}$ variability

Contoured maps show that $\delta^{13}C_{org}$ values are at their lowest (<-31‰) in central regions of the deep-water shelf, with a gradual increase toward the inner shelf edges, thereby forming a nearshore-to-offshore $\delta^{13}C_{org}$ gradient of up to 4‰ (Fig. 4). The gradient is most pronounced around the southwest edges of the shelf, where dense $\delta^{13}C_{org}$ contours extend broadly along the shoreline. In the central shelf regions, $\delta^{13}C_{org}$ values exhibit minor variations between -30‰ and -31‰.

The $\delta^{13}C_{org}$ value of marine sediments can be influenced by various factors, including biological and thermal degradation, isotopic fractionation during primary production, terrestrial organic carbon input, and hydrocarbon contamination (Meyers, 1994; Popp et al., 1998; Jiang et al., 2012; Oehlert and Swart, 2014). Among these factors, the thermal maturation of organic matter would cause the loss of isotopically light ^{12}C and the enrichment of ^{13}C (Watanabe et al., 1997; Jiang et al., 2012). However, the potential effects of thermal maturation typically result in a $\delta^{13}C_{org}$ shift of 2–3‰, which is insufficient to account for the observed maximum variability of ca. 4‰. Moreover, the thermal maturity of organic matter does not exhibit a clear increasing offshore-to-nearshore trend that would result in elevated $\delta^{13}C_{org}$ values in nearshore regions of the Yangtze Shelf (Wang et al., 2019; Luo et al., 2025). Thus, the thermal degradation of organic matter is unlikely to be the primary driver for the spatial variability in $\delta^{13}C_{org}$ on the shelf. This is also supported by the lack of correlation between TOC and $\delta^{13}C_{org}$ in both Wanhe (R^2 = 0.18; Fig. S4A) and Shuanghe (R^2 = 0.07; Fig. S4B) samples, except for pure limestones of the Pagoda and

Linhsiang formations, which have extremely low TOC values.

In addition, while hydrocarbon contamination can locally alter $\delta^{13}C_{org}$ values (Jiang et al., 2012), it is unlikely to account for the consistent, shelf-wide $\delta^{13}C_{org}$ variability observed in each time slice. Moreover, $\delta^{13}C_{org}$ values of bitumen (>-29‰) in Phanerozoic reservoir rocks in the Sichuan Basin are generally higher than the $\delta^{13}C_{org}$ values (< -31‰) in the hydrocarbon-rich central shelf. Thus, hydrocarbon contamination is also unlikely to be the primary control on the broad $\delta^{13}C_{org}$ spatial patterns.

During the Ordovician–Silurian transition, the Yangtze Shelf Sea was situated in the tropical zone (Fig. 2A), with very little lateral variation in sea surface temperature (Bergmann et al., 2025). Therefore, seawater temperature differences are unlikely to have caused the observed $\delta^{13}C_{org}$ patterns. Although the potential influence of differences in isotopic fractionation among primary producers cannot be ruled out, it is more likely that the systematic spatial variability in $\delta^{13}C_{org}$ reflects, at least in part, a shelf-scale heterogeneity in seawater $\delta^{13}C_{DIC}$ values (LaPorte et al., 2009; Ahm et al., 2017; Yang et al., 2024). This interpretation aligns with previous findings from Late Ordovician epeiric seas in Laurentia, where lateral $\delta^{13}C_{org}$ variability has been attributed to regional variability in seawater DIC (e.g., Panchuk et al., 2005; Melchin and Holmden, 2006; LaPorte et al., 2009). To investigate the plausibility of seawater $\delta^{13}C_{DIC}$ variability on the Yangtze Shelf, we further examine $\delta^{13}C_{carb}$ records from the Wanhe and Shuanghe sections.

5.2 $\delta^{13}C_{carb}$ records of seawater $\delta^{13}C_{DIC}$ variability

Our results show that $\delta^{13}C_{carb}$ values at Wanhe vary across a wide range of ca. 4.2‰, whereas those at Shuanghe show a narrower range of ca. 2.6‰ (Fig. 3). Notably, the magnitude of $\delta^{13}C_{carb}$ variation at Wanhe is comparable to the ~4‰ nearshore-to-offshore $\delta^{13}C_{org}$ gradient across the Yangtze Shelf (Fig. 4). However, mineralogical and diagenetic factors may potentially influence the fidelity of $\delta^{13}C_{carb}$ records as indicators of original seawater $\delta^{13}C_{DIC}$ (Ahm et al., 2018; Higgins et al., 2018; Jones et al., 2020). In addition, changes in faunal community structure and seawater temperature may also affect original $\delta^{13}C_{carb}$ and $\delta^{44}Ca$ values in sediments (Romanek et al., 1992; Gussone et al., 2020). However, these primary signals are often overprinted by early marine diagenesis and are thus difficult to isolate with confidence. In the following discussion, we assess the potential influence of mineralogical and diagenetic processes on the preservation of primary $\delta^{13}C_{carb}$ signals using paired $\delta^{13}C_{carb}$ and $\delta^{44}Ca$ measurements and numerical models. The remaining $\delta^{13}C_{carb}$ variability that cannot be explained by mineralogical changes or diagenetic overprints is considered to reflect changes in regional seawater $\delta^{13}C_{DIC}$ or broader perturbations to the global carbon cycle.

5.2.1 Mineralogical effects

Although the Ordovician-Silurian ocean is traditionally considered to have been a "calcite sea" (Hardie, 1996), this does not preclude local or regional precipitation of aragonite on the warm, low-latitude Yangtze Shelf Sea (Finnegan et al., 2011;

Bergmann et al., 2025). Previous studies have also proposed the production of aragonite in shallow marine environments during this time (Kimmig and Holmden, 2017; Jones et al., 2020; Adiatma et al., 2024). Our $\delta^{44}Ca$ data from both the Wanhe (-1.41‰ to -0.93‰) and Shuanghe (-1.57‰ to -0.87‰) sections consistently fall between the isotopic ranges of primary aragonite (-1.1‰ to -1.7‰) and calcite (-0.8‰ to -1.3‰) end members (Holmden et al., 2024), suggesting that the observed stratigraphic variability in $\delta^{44}Ca$ may reflect depositional mixing of aragonite and calcite in different proportions (Adiatma et al., 2024). This is also supported by a broadly negative covariation between Sr/Ca and $\delta^{44}Ca$ at Wanhe (R^2 = 0.17; Fig. S5), as primary aragonite is characterized by higher Sr/Ca ratios and lower $\delta^{44}Ca$ values relative to primary calcite (Gussone et al., 2020). We use the simple two-end member mixing model of Adiatma et al. (2024) to estimate the potential influence of primary mineralogy on both $\delta^{44}Ca$ and $\delta^{13}C_{carb}$ for our samples (Fig. 5). The model is defined by the equation:

$$R_{carb} = R_{arag} f_{arag} \frac{C_{arag}}{C_{carb}} + R_{calc} f_{calc} \frac{C_{calc}}{C_{carb}}$$

where R_x and f_x represent the isotopic ratios and mixing fractions of each carbonate end member, respectively, and C_x is the element concentration (e.g., Ca, C) within carbonate minerals. The subscripts refer to bulk carbonate (carb), aragonite end member (arag), and calcite end member (calc). For the $\delta^{44}Ca$ model (Fig. 5A), we apply isotopic offsets of -1.5‰ for aragonite and -0.9‰ for calcite relative to seawater (Gussone et al., 2020). The seawater $\delta^{44}Ca$ value is estimated to range from -0.7‰ to

-0.25‰ during the Ordovician–Silurian transition (Holmden et al., 2024). For the $\delta^{13}C$ mixing model (Fig. 5B), isotopic offsets relative to seawater DIC are set to 2.7‰ for aragonite and 1.0‰ for calcite (Romanek et al., 1992). To reproduce the lowest $\delta^{13}C_{carb}$ value (-2.37‰) in the 100% calcite endmember and the highest $\delta^{13}C_{carb}$ value (1.83‰) in the 100% aragonite endmember, two threshold seawater $\delta^{13}C_{DIC}$ values of -3.37‰ and -0.87‰ are adopted.

The modeling results show that the range of measured $\delta^{44}Ca$ and $\delta^{13}C_{carb}$ values from the Wanhe and Shuanghe sections falls beyond the theoretical aragonite-calcite mixing lines (Fig. 5). If we assume a constant Ca isotopic offset between carbonate minerals and seawater, and no diagenetic alteration, the measured $\delta^{44}Ca$ range (-1.57‰ to -0.87‰) would require a seawater $\delta^{44}Ca$ value of ~0‰. However, the $\delta^{44}Ca$ value of normal marine seawater during the Ordovician– Silurian transition is estimated to have been ~-0.5‰ (Holmden et al., 2024), with elevated $\delta^{44}Ca$ values (up to -0.25‰) observed only in highly evaporated seawater (Holmden, 2009). Given that the Yangtze Shelf Sea was open to the global ocean (as evidenced by the widespread distribution of cosmopolitan graptolites; Chen et al., 2005), a seawater $\delta^{44}Ca$ value as high as ~0‰ was unlikely. Although tropical sea-surface temperature fluctuated by up to ~10°C across the Hirnantian glaciation (Finnegan et al., 2011), Ca isotopes exhibit low temperature sensitivity (generally < 0.03‰/°C; Gussone et al., 2020). Furthermore, lower temperatures generally increase the isotopic offset between carbonate minerals and seawater (Gussone et al., 2020). Consequently, glacial cooling would enhance this

offset, causing the theoretical aragonite-calcite mixing lines to be even further from the measured $\delta^{44}Ca$ values. These observations suggest that changes in primary mineralogy alone are insufficient to explain the $\delta^{44}Ca$ trends in our sections. Similarly, reproducing the measured $\delta^{13}C_{carb}$ range (-2.37‰ to 1.83‰) would require variable seawater $\delta^{13}C_{DIC}$ from -3.37‰ to -0.87‰ (Fig. 5B), suggesting that mineralogical changes also cannot account for the observed $\delta^{13}C_{carb}$ variability.

5.2.2 Early marine diagenesis

Early marine diagenesis is an alternative process that can alter original $\delta^{13}C_{carb}$ and $\delta^{44}Ca$ signals in carbonate sediments (Ahm et al., 2018; Higgins et al., 2018; Gussone et al., 2020; Jones et al., 2020). In shallow-water environments, carbonate sediments commonly undergo fluid-buffered diagenetic alteration, characterized by extensive exchange between porewater and seawater, resulting in isotopic equilibrium between diagenetic carbonate minerals and seawater (Hoffman and Lamothe, 2019; Holmden et al., 2024). In such systems, $\delta^{44}Ca$ values of diagenetic minerals increase toward contemporaneous seawater values, while Sr/Ca and U/Ca ratios typically decrease relative to primary aragonite or calcite (Holmden, 2009; Busch et al., 2022; Holmden et al., 2024). By contrast, in relative deep-water settings, primary $\delta^{44}Ca$ signatures are more likely to be preserved during early marine diagenesis (Holmden et al., 2024). This preservation is attributed to sluggish porewater circulation under sediment-buffered conditions, in which most of the re-precipitated Ca is sourced from the primary carbonate minerals (Hoffman and Lamothe, 2019; Holmden et al., 2024).

Based on this interpretive framework, the geochemical signals from the Wanhe and Shuanghe sections indicate different diagenetic conditions. Shallow-water limestones, characterized by high $\delta^{44}Ca$ and low Sr/Ca and U/Ca ratios (Fig. S6), likely experienced fluid-buffered diagenesis. By contrast, calcareous shales deposited in relatively deep-water settings, exhibiting low $\delta^{44}Ca$ and high Sr/Ca and U/Ca ratios, appear to have undergone sediment-buffered early marine diagenesis.

To further assess the influence of early marine diagenesis on our $\delta^{44}Ca$ and $\delta^{13}C$ data, we apply a numerical model developed by Ahm et al. (2018). This model includes a series of boxes (box 1 to box n), each representing a segment of porous sediment, and simulates the recrystallization of aragonite to low-Mg calcite (neomorphism) or aragonite/calcite to dolomite (dolomitization) as fluid flows along the path from box 1 (fluid-buffered) to box n (sediment-buffered). Given that one-third of our samples have higher carbonate Sr/Ca ratios than typical primary calcite (~1 mmol/mol), and considering that early marine diagenesis generally decreases carbonate Sr/Ca ratios (Tang et al., 2008; Gussone et al., 2016; Ahm et al., 2018), we assume a primary mineralogy of 100% aragonite in our model setup. Our measured carbonate Mg/Ca ratios (<0.01 to 0.85 mol/mol; Table S1) range from values typical of low-Mg calcite to those approaching stoichiometric dolomite, suggesting that both calcite and dolomite likely formed during early marine diagenesis. To reproduce the lightest $\delta^{13}C_{carb}$ value in our data (-2.37‰) in the 100% calcite endmember, we set the $\delta^{13}C$ value of initial diagenetic fluid (i.e., seawater) to -3.4‰. The $\delta^{13}C$ value of primary

sediment is set at 2‰ based on the highest $\delta^{13}C_{carb}$ value of 1.83‰ in our data. The $\delta^{44}Ca$ of the diagenetic fluid is set at -0.5‰, consistent with normal marine seawater during the Ordovician–Silurian transition. All other parameters are set to their default values as listed in Table 1.

Model results indicate that nearly all data points from the Wanhe and Shuanghe sections fall within the predicted fields representing>80% diagenetic alteration in the cross-plot of Sr/Ca ratios versus $\delta^{44}Ca$ values (Fig. 6). This suggests that the variability in carbonate Sr/Ca and $\delta^{44}Ca$ data for our samples can be attributed to neomorphism or dolomitization of aragonite during early marine diagenesis (Ahm et al., 2018; Adiatma et al., 2024). By contrast, in the cross-plot of $\delta^{13}C_{carb}$ and $\delta^{44}Ca$ (Fig. 7A), only about one-third of data points (33 out of 80; Table S1) fall within the predicted fields of modeling Scenario A, which represents our best estimate of the $\delta^{13}C$ value of the initial diagenetic fluid (-3.4‰). This observation suggests that early marine diagenesis alone cannot fully account for the range of $\delta^{13}C_{carb}$ values.

Departures of data points from the modeled fields have been interpreted to reflect spatio-temporal heterogeneity in the geochemistry of the diagenetic fluid or the primary carbonate mineral (Crockford et al., 2020; Adiatma et al., 2024). To best capture the range of the measured $\delta^{13}C_{carb}$ data, we also consider Scenario B (Fig. 7B), which assumes a lighter $\delta^{13}C$ value of ~-9‰ for the initial diagenetic fluid (i.e., seawater). Extremely light seawater $\delta^{13}C_{DIC}$ values have been reported in the modern Florida Bay, where local seawater $\delta^{13}C_{DIC}$ can be as low as -7‰ due to respiration of

^{13}C-depleted terrestrial organic carbon ($\delta^{13}C \approx -25‰$) and restricted circulation (Patterson and Walter, 1994). However, such a scenario is highly unlikely for the open Yangtze Shelf Sea during the Ordovician–Silurian transition. This inference is supported by higher $\delta^{13}C_{org}$ values observed in nearshore areas (Fig. 4), which imply a negligible contribution of terrestrial organic matter to marine C cycling, even though vascular plants may have colonized the land by this time (Lenton et al., 2012; Jones et al., 2015). Moreover, previous studies on biomarkers and kerogen macerals show that organic matter in the Late Ordovician and early Silurian successions on the Yangtze Shelf was largely derived from marine organisms (e.g., algae, bacteria, graptolites), with no apparent terrestrial signals (e.g., Qiu et al., 2022a; Liang et al., 2024; Luo et al., 2025). In summary, although Scenario B improves the model fit to our measured data (77 out of 80; Fig. 7B), it may be less representative of typical diagenetic conditions during the Ordovician–Silurian transition.

5.3 Sea level controls on $\delta^{13}C_{DIC}$ variability in shelf seawater

As discussed above, the $\delta^{13}C_{carb}$ variability in the Wanhe and Shuanghe sections can be partially attributed to changes in primary mineralogy and early marine diagenesis. The remaining $\delta^{13}C_{carb}$ variability, unexplained by these two factors, most likely records heterogeneity in primary $\delta^{13}C_{carb}$ values of shelf sediments, which in turn indicates spatio-temporal variability in marine $\delta^{13}C_{DIC}$ (Crockford et al., 2020; Adiatma et al., 2024). This interpretation is consistent with the significant $\delta^{13}C_{org}$ variability observed across the Yangtze Shelf (Fig. 4), and also agrees with previous studies

documenting spatial differences in seawater $\delta^{13}C_{DIC}$ values in Late Ordovician epeiric seas (e.g., Panchuk et al., 2005; Melchin and Holmden, 2006; LaPorte et al., 2009; Ahm et al., 2017). Elevated $\delta^{13}C_{carb}$ values in shallow-water carbonates, together with the observed nearshore-to-offshore $\delta^{13}C_{org}$ gradient across the shelf (Fig. 4), suggest higher seawater $\delta^{13}C_{DIC}$ values in nearshore regions. This marine $\delta^{13}C_{DIC}$ pattern potentially results from (1) high rates of photosynthesis (preferentially utilizing light ^{12}C) driven by an abundant supply of terrestrial nutrients (e.g., LaPorte et al., 2009; Qiu et al., 2022b), and (2) restricted DIC exchange with the open ocean (e.g., Fanton and Holmden, 2007).

The pronounced differences in $\delta^{13}C_{org}$ patterns before (Fig. 4C), during (Fig. 4D) and after (Fig. 4E) the glacial maximum imply a potential link between marine $\delta^{13}C_{DIC}$ changes and sea-level fluctuations. To further illustrate this, we have reconstructed the relative sea-level history of the Wanhe and Shuanghe sections (Fig. 3). Overall, shale facies with low Ti/Al, Zr/Al, Al+K+Ti, bulk Ca (Ca_{bulk}) and carbonate Ca (Ca_{carb}) concentrations are interpreted to reflect rising sea-level and associated carbonate-platform drowning (Fanton and Holmden, 2007; Li et al., 2021). In the Daduhe Formation of the Wanhe section, sea-level fluctuations correlate well with the 405-thousand-year Milankovitch cycles (Zhong et al., 2020), and are comparable to long-term transgression– regression cycles in the coeval Wufeng Formation of the Shuanghe section (Fig. S7).

The Daduhe Formation in the Wanhe section exhibits a series of short-term

$\delta^{13}C_{org}$ shifts that are broadly consistent with relative sea-level changes (Fig. 3A). Specifically, negative $\delta^{13}C_{org}$ shifts occur during intervals of rising sea level, while positive $\delta^{13}C_{org}$ shifts occur during falling sea level. Given that higher $\delta^{13}C_{org}$ values (>-30‰) occur in shallow-water carbonates, and lower $\delta^{13}C_{org}$ values (<-30‰) are found in deeper-water shales, these short-term $\delta^{13}C_{org}$ shifts likely reflect local marine DIC changes driven by relative sea level, rather than global C-cycle perturbations. This notion is supported by consistently low $\delta^{13}C_{org}$ values in the contemporaneous, persistently deep-water Wufeng Formation at Shuanghe (Fig. 3B). By contrast, the Daduhe Formation records fluctuations between a shallower carbonate platform and a deeper siliceous shelf, each with a distinct $\delta^{13}C_{DIC}$ value. As a result, regional transgressions and regressions resulted in alternating negative and positive $\delta^{13}C_{org}$ shifts in the Daduhe Formation.

5.4 Implications for the HICE

Our compilation of 7 deep marine and 38 shelf sites shows that the onset of the HICE coincides with a notable increase in TOC concentrations (especially in the Yangtze Shelf; Fig. 1D) in the latest Katian, supporting the hypothesis that substantial organic carbon burial triggered the HICE (Brenchley et al., 1994; Zhang et al., 2024). Notably, the signal of increased organic carbon burial is not captured in estimates of organic carbon accumulation rate (OCAR) averaged across individual graptolite zones (Yang and Fan, 2025). Because the duration of a graptolite zone can exceed 2 Ma (e.g., *Paraorthograptus pacificus* Zone; Cooper et al., 2012), high OCAR values from

shorter, organic-rich intervals are likely diluted by longer, organic-poor intervals within the same graptolite zone, thereby obscuring short-term signals of increased organic carbon burial.

The increased organic carbon burial in the latest Katian oceans could be attributed to a combination of two key factors: (i) enhanced primary productivity driven by increased nutrient supply from extensive volcanism and intense sedimentary phosphorus recycling (Longman et al., 2021; Qiu et al., 2022b), and (ii) widespread ocean anoxia that facilitated the preservation of organic matter in sediments (Hammarlund et al., 2012; Zou et al., 2018; Dahl et al., 2021). Additionally, glacial deposits on high-latitude continents suggest that the Hirnantian glaciation likely began in the latest Katian (Ghienne et al., 2014), broadly coinciding with elevated TOC values and the onset of the HICE in global records (Fig. 1). In addition, ocean cooling associated with glaciation may have reduced organic carbon remineralization rates by lowering aerobic respiration rates in the water column, thereby enhancing the preservation efficiency of organic matter in sediments (Jones and Fike, 2013). This cooling-driven mechanism provides an alternative or complementary pathway for increased organic carbon burial that triggered the HICE.

It is worth noting that TOC and $\delta^{13}C$ are out of step during the HICE, since TOC decreases as $\delta^{13}C$ rises to its maximum across multiple sections from different continents (Fig. 1A-D). This decoupling likely reflects a decline in organic carbon burial, potentially driven by progressive ocean oxygenation associated with the

Hirnantian glaciation. Enhanced ocean circulation during the glacial period may have introduced polar-derived, oxygen-rich waters into previously anoxic environments (Yan et al., 2012; Zou et al., 2018), thereby increasing organic carbon remineralization rates in the water column. The sustained positive shift in both $\delta^{13}C_{carb}$ and $\delta^{13}C_{org}$ records, despite reduced organic carbon burial, suggests that additional drivers played an important role in modulating marine $\delta^{13}C_{DIC}$ values across the Hirnantian glaciation.

Given the significant spatial variability in marine $\delta^{13}C_{DIC}$ across the Yangtze Shelf, as indicated by our $\delta^{13}C_{org}$ time slices, we infer that regional factors may have also contributed to the HICE. To test this hypothesis, we mapped the HICE amplitudes ($\Delta^{13}C_{org}$) extracted from 10% LOWESS fitted $\delta^{13}C_{org}$ curves. The resulting $\Delta^{13}C_{org}$ map shows that the HICE amplitudes are higher on the northeast edge of the shelf sea, with lower values in central shelf regions (Fig. 8A), highlighting considerable spatial heterogeneity in marine $\delta^{13}C_{DIC}$ changes across the Hirnantian glaciation. The spatial heterogeneity observed in the $\Delta^{13}C_{org}$ map cannot be readily explained by organic carbon burial alone, further supporting the inference that regional drivers played an important role in the sustained positive shift in marine $\delta^{13}C_{DIC}$ values.

The apparent retreat of $\delta^{13}C_{org}$ contours towards offshore regions during glacioeustatic sea-level fall (Fig. 4D) supports the hypothesis that sea-level change drove the progressive $\delta^{13}C_{DIC}$ excursion in the Hirnantian ocean (Panchuk et al., 2005; LaPorte et al., 2009; Ahm et al., 2017; Jones et al., 2020). In this hypothesis, the regression caused $\delta^{13}C_{DIC}$ signals in more offshore areas to develop to higher values

typical of shallower settings. Given the distinct timing and magnitude of responses to regression in different regions of the shelf, as indicated by the spatially variable thickness of the Hirnantian Kuanyinchiao Bed (Text S2 and Fig. S8), changes in the marine $\delta^{13}C_{DIC}$ signals exhibit temporal and spatial variability.

We also note anomalously large $\Delta^{13}C_{org}$ values around the Central Guizhou Uplift and on the shelf edge north of the Yichang Uplift (Fig. 8A), where Late Ordovician carbonate rocks were exposed and eroded during the glacial maximum (Fig. 8B; Chen et al., 2001, 2018). Similar weathering of exposed carbonates also occurred on other low-latitude continents during the Hirnantian glaciation (e.g., Finney et al., 1999; Kiipli and Kiipli, 2020). The weathering of emergent marine carbonates would increase input fluxes of dissolved Ca, even during the glacial interval when weathering rates were low. Previous studies suggest that, during the Hirnantian glaciation, the water column above slope and deep marine sediments was near to saturation or oversaturated with respect to $CaCO_3$, likely due to (i) glacioeustatic sea-level fall forcing carbonate deposition offshore, and/or (ii) increased alkalinity from the weathering of exposed marine carbonates (Koehler et al., 2019). This is consistent with the significant increases in carbonate content and Ca/Al ratios in global outer shelf and deep-marine sections during the HICE interval (Fig. 1E). Furthermore, the weathering of emergent marine carbonates would have enhanced the flux of isotopically heavier ^{13}C into the ocean, as platform carbonates have higher $\delta^{13}C$ values relative to contemporaneous seawater DIC (Romanek et al., 1992). This can explain the elevated $\delta^{13}C_{org}$ and $\Delta^{13}C_{org}$

values around the Central Guizhou and Yichang uplifts (Fig. 4D and Fig. 8A), where marine carbonate rocks were weathered during the Hirnantian glacial, as indicated by the erosional surface and sedimentary hiatus above the Pagoda– Linhsiang limestones (Fig. 8B; Chen et al., 2001).

While weathered-C input likely intensified the spatial heterogeneity of marine $\delta^{13}C_{DIC}$ values locally, its impact on offshore marine DIC reservoirs, more distal to emergent marine carbonates, may have been relatively limited. This inference is supported by the moderate $\delta^{13}C_{org}$ excursions (<+2‰) in the central deep-water shelf (Fig. 8A), and is consistent with an estimated ~1.5‰ $\delta^{13}C$ perturbation on average in the global ocean (Ahm et al., 2017). Therefore, we conclude that global carbon cycle perturbations associated with the Hirnantian glaciation were of smaller amplitude than the $\delta^{13}C$ changes observed in some local records, highlighting the need for caution when reconstructing global carbon cycle perturbations from regional datasets during other carbon isotope excursion events through Earth's history.

6. Conclusions

This study documents a nearshore-to-offshore $\delta^{13}C_{org}$ gradient of up to 4‰ across the Yangtze Shelf during the Ordovician–Silurian transition. To evaluate whether this gradient reflects spatial variability in contemporaneous seawater $\delta^{13}C_{DIC}$ values, we report $\delta^{13}C_{carb}$, $\delta^{44}Ca$ and Sr/Ca data from the shallow-water Wanhe and deep-water Shuanghe sections. Model results suggest that part of the observed $\delta^{13}C_{carb}$ variability in our data can be attributed to changes in primary mineralogy and early marine

diagenesis. However, the remaining $\delta^{13}C_{carb}$ variability most likely reflects shelf-scale heterogeneity in marine $\delta^{13}C_{DIC}$ values, which closely parallels the spatial patterns observed in $\delta^{13}C_{org}$ records. Although enhanced organic carbon burial likely triggered the HICE, the magnitude of this excursion is strongly controlled by regional sea-level fall, which drove asynchronous and spatially heterogeneous changes in marine $\delta^{13}C_{DIC}$ signals. Carbonate weathering further contributed to the observed spatial heterogeneity in marine $\delta^{13}C_{DIC}$, especially in near-shore areas. Our study highlights the importance of regional and local controls on marine $\delta^{13}C_{DIC}$ changes and indicates that global C-cycle perturbations during the Hirnantian glaciation were much smaller than a simple reading of the carbon isotope record implies.

CRediT authorship contribution statement

Jiaqiang Zhang: Writing – review & editing, Writing – original draft, Visualization, Methodology, Investigation, Formal analysis, Conceptualization. **Zhen Qiu:** Writing – review & editing, Writing – original draft, Investigation, Methodology, Formal analysis, Validation, Funding acquisition, Supervision, Project administration. **Wenjiao Xiao**: Writing – review&editing, Formal analysis, Funding acquisition, Supervision, Project administration. **Paul B. Wignall:** Writing – review&editing, Formal analysis, Conceptualization, Supervision. **Weiliang Kong:** Writing – review&editing, Methodology, Investigation, Formal analysis. **Benjamin J. W. Mills:** Writing – review&editing, Formal analysis. **Yijun Xiong**: Writing – review & editing, Methodology,

Formal analysis. **Simon W. Poulton**: Writing – review&editing, Formal analysis, Conceptualization, Supervision.

Declaration of competing interest

The authors declare that they have no known competing financial interests or personal relationships that could have appeared to influence the work reported in this paper.

Supplementary material

Supplementary material related to this article can be found on-line at XXX

Acknowledgments

This work was funded by the National Natural Science Foundation of China (grants 42222209 and 42488201), the Scientific Research and Technological Development Programs of CNPC (grant 2021yjcq02), and the State Scholarship Fund. We thank Hengye Wei and J. Smolarek-Lach for sampling and data sharing, and Linhao Fang and Yinggang Zhang for valuable discussion. We are also grateful to Editor Dr. Tristan Horner and anonymous reviewers for their constructive comments and suggestions that greatly improved the manuscript.

References

Adiatma, Y.D., Saltzman, M.R., Griffith, E.M., 2024. Calcium isotope constraints on a Middle Ordovician carbon isotope excursion. Earth Planet Sci. Lett. 641, 118805.

Ahm, A.-S.C., Bjerrum, C.J., Blättler, C.L., Swart, P.K., Higgins, J.A., 2018. Quantifying early marine diagenesis in shallow-water carbonate sediments. Geochim. Cosmochim. Acta 236, 140–159.

Ahm, A.-S.C., Bjerrum, C.J., Hammarlund, E.U., 2017. Disentangling the record of diagenesis, local redox conditions, and global seawater chemistry during the latest Ordovician glaciation. Earth Planet. Sci. Lett. 459, 145–156.

Bergmann, K.D., Macdonald, F.A., Swanson-Hysell, N.L., 2025. The Causes and Consequences of Ordovician Cooling. Annu. Rev. Earth Planet. Sci. 53, 651–685.

Brenchley, P.J., Marshall, J.D., Carden, G.A.F., Robertson, D.B.R., Long, D.G.F., Meidla, T., Hints, L., Anderson, T.F., 1994. Bathymetric and isotopic evidence for a short-lived Late Ordovician glaciation in a greenhouse period. Geology 22, 295–298.

Busch, J.F., Hodgin, E.B., Ahm, A.-S.C., Husson, J.M., Macdonald, F.A., Bergmann, K.D., Higgins, J.A., Strauss, J.V., 2022. Global and local drivers of the Ediacaran Shuram carbon isotope excursion. Earth Planet. Sci. Lett. 579, 117368.

Chen, X., Chen, Q., Zhen, Y., Wang, H., Zhang, L., Zhang, J., Wang, W., Xiao, Z., 2018. Circumjacent distribution pattern of the Lungmachian graptolitic black shale (early Silurian) on the Yichang Uplift and its peripheral region. Sci. China-Earth Sci. 61,

1195–1203.

Chen, X., Fan, J., Chen, Q., Tang, L., Hou, X., 2014. Toward a stepwise Kwangsian Orogeny. Sci. China-Earth Sci. 57, 379–387.

Chen, X., Rong, J., Fan, J., Zhan, R., Charles, E.M., David, A.T.H., Michael, J.M., Stan, C.F., Wang, X., 2006. The Global Boundary Stratotype Section and Point (GSSP) for the base of the Hirnantian Stage (the uppermost of the Ordovician System). Episodes 29, 183–196.

Chen, X., Melchin, M.J., Sheets, H.D., Mitchell, C.E., Fan, J.-X., 2005. Patterns and processes of latest Ordovician graptolite extinction and recovery based on data from South China. J. Paleontol. 79, 842–861.

Chen, X., Rong, J., Zhou, Z., Zhang, Y., Zhan, R., Liu, J., Fan, J., 2001. The Central Guizhou and Yi-chang uplifts, Upper Yangtze region, between Ordovician and Silurian. Chin. Sci. Bull. 46, 1580–1584.

Cocks, L.R.M., Torsvik, T.H., 2021. Ordovician palaeogeography and climate change. Gondwana Res. 100, 53–72.

Cooper, R.A., Sadler, P.M., Hammer, O., Gradstein, F.M., 2012. Chapter 20 - The Ordovician Period, in: Gradstein, F.M., Ogg, J.G., Schmitz, M.D., Ogg, G.M. (Eds.), The Geologic Time Scale. Elsevier, Boston, pp. 489–523.

Crockford, P.W., Kunzmann, M., Blättler, C.L., Kalderon-Asael, B., Murphy, J.G., Ahm, A.-S., Sharoni, S., Halverson, G.P., Planavsky, N.J., Halevy, I., Higgins, J.A., 2020. Reconstructing Neoproterozoic seawater chemistry from early diagenetic

dolomite. Geology 49, 442–446.

Dahl, T.W., Hammarlund, E.U., Rasmussen, C.M.Ø., Bond, D.P.G., Canfield, D.E., 2021. Sulfidic anoxia in the oceans during the Late Ordovician mass extinctions – insights from molybdenum and uranium isotopic global redox proxies. Earth Sci. Rev. 103748.

Deng, Y., Fan, J., Zhang, S., Fang, X., Chen, Z., Shi, Y., Wang, H., Wang, X., Yang, J., Hou, X., Wang, Y., Zhang, Y., Chen, Q., Yang, A., Fan, R., Dong, S., Xu, H., Shen, S., 2021. Timing and patterns of the Great Ordovician Biodiversification Event and Late Ordovician mass extinction: Perspectives from South China. Earth Sci. Rev. 220, 103743.

Fanton, K.C., Holmden, C., 2007. Sea-level forcing of carbon isotope excursions in epeiric seas: implications for chemostratigraphy. Can. J. Earth Sci. 44, 807–818.

Finnegan, S., Bergmann, K., Eiler, J.M., Jones, D.S., Fike, D.A., Eisenman, I., Hughes, N.C., Tripati, A.K., Fischer, W.W., 2011. The magnitude and duration of Late Ordovician-Early Silurian glaciation. Science 331, 903–906.

Finney, S.C., Berry, W.B.N., Cooper, J.D., Ripperdan, R.L., Sweet, W.C., Jacobson, S.R., Soufiane, A., Achab, A., Noble, P.J., 1999. Late Ordovician mass extinction: A new perspective from stratigraphic sections in central Nevada. Geology 27, 215–218.

Ghienne, J.-F., Desrochers, A., Vandenbroucke, T.R.A., Achab, A., Asselin, E., Dabard, M.-P., Farley, C., Loi, A., Paris, F., Wickson, S., Veizer, J., 2014. A Cenozoic-style scenario for the end-Ordovician glaciation. Nat. Commun. 5, 4485.

669 Gussone, N., Ahm, A.-S.C., Lau, K.V., Bradbury, H.J., 2020. Calcium isotopes in deep
670 time: Potential and limitations. Chem. Geol. 544, 119601.
671 Hammarlund, E.U., Dahl, T.W., Harper, D.A.T., Bond, D.P.G., Nielsen, A.T., Bjerrum, C.J.,
672 Schovsbo, N.H., Schönlaub, H.P., Zalasiewicz, J.A., Canfield, D.E., 2012. A sulfidic
673 driver for the end-Ordovician mass extinction. Earth Planet. Sci. Lett. 331–332,
674 128–139.
675 Hardie, L.A., 1996. Secular variation in seawater chemistry: An explanation for the
676 coupled secular variation in the mineralogies of marine limestones and potash
677 evaporites over the past 600 m.y. Geology 24, 279–283.
678 Harper, D.A.T., 2023. Late Ordovician Mass Extinction: Earth, fire and ice. Natl. Sci.
679 Rev. 11, nwad319.
680 Higgins, J.A., Blättler, C.L., Lundstrom, E.A., Santiago-Ramos, D.P., Akhtar, A.A., Crüger
681 Ahm, A.S., Bialik, O., Holmden, C., Bradbury, H., Murray, S.T., Swart, P.K., 2018.
682 Mineralogy, early marine diagenesis, and the chemistry of shallow-water
683 carbonate sediments. Geochim. Cosmochim. Acta 220, 512–534.
684 Hoffman, P.F., Lamothe, K.G., 2019. Seawater-buffered diagenesis, destruction of
685 carbon isotope excursions, and the composition of DIC in Neoproterozoic oceans.
686 Proc. Natl. Acad. Sci. 116, 18874–18879.
687 Holmden, C., Kimmig, S.R., Nadeau, M.D., 2024. Ca isotopic gradients in epeiric marine
688 carbonates: Diagenetic origins of and significance for Ca cycle reconstructions.
689 Geochim. Cosmochim. Acta 373, 151–168.

690 Holmden, C., 2009. Ca isotope study of Ordovician dolomite, limestone, and anhydrite
691 in the Williston Basin: Implications for subsurface dolomitization and local Ca
692 cycling. Chem. Geol. 268, 180–188.
693 Jiang, G., Wang, X., Shi, X., Xiao, S., Zhang, S., Dong, J., 2012. The origin of decoupled
694 carbonate and organic carbon isotope signatures in the early Cambrian (ca. 542–
695 520Ma) Yangtze platform. Earth Planet. Sci. Lett. 317–318, 96–110.
696 Jin, X., Pan, C., Yu, S., Li, E., Wang, J., Fu, X., Qin, J., Xie, Z., Zheng, P., Wang, L., Chen, J.,
697 Tan, Y., 2014. Organic geochemistry of marine source rocks and
698 pyrobitumen-containing reservoir rocks of the Sichuan Basin and neighbouring
699 areas, SW China. Mar. Pet. Geol. 56, 147–165.
700 Jones, D.S., Brothers, R.W., Crüger Ahm, A.-S., Slater, N., Higgins, J.A., Fike, D.A., 2020.
701 Sea level, carbonate mineralogy, and early diagenesis controlled $\delta^{13}C$ records in
702 Upper Ordovician carbonates. Geology 48, 194–199.
703 Jones, D.S., Creel, R.C., Rios, B., Santiago Ramos, D.P., 2015. Chemostratigraphy of an
704 Ordovician–Silurian carbonate platform: $\delta^{13}C$ records below glacioeustatic
705 exposure surfaces. Geology 43, 59–62.
706 Jones, D.S., Fike, D.A., 2013. Dynamic sulfur and carbon cycling through the
707 end-Ordovician extinction revealed by paired sulfate–pyrite $\delta^{34}S$. Earth Planet Sci.
708 Lett. 363, 144–155.
709 Kiipli, E., Kiipli, T., 2020. Hirnantian sea-level changes in the Baltoscandian Basin, a
710 review. Palaeogeogr. Palaeoclimatol. Palaeoecol. 540, 109524.

711 Kimmig, S.R., Holmden, C., 2017. Multi-proxy geochemical evidence for primary
712 aragonite precipitation in a tropical-shelf ‘calcite sea’ during the Hirnantian
713 glaciation. Geochim. Cosmochim. Acta 206, 254–272.
714 Koehler, M.C., Stüeken, E.E., Hillier, S., Prave, A.R., 2019. Limitation of fixed nitrogen
715 and deepening of the carbonate-compensation depth through the Hirnantian at
716 Dob's Linn, Scotland. Palaeogeogr. Palaeoclimatol. Palaeoecol. 534, 109321.
717 Kump, L.R., Arthur, M.A., Patzkowsky, M.E., Gibbs, M.T., Pinkus, D.S., Sheehan, P.M.,
718 1999. A weathering hypothesis for glaciation at high atmospheric pCO_2 during the
719 Late Ordovician. Palaeogeogr. Palaeoclimatol. Palaeoecol. 152, 173-187.
720 LaPorte, D.F., Holmden, C., Patterson, W.P., Loxton, J.D., Melchin, M.J., Mitchell, C.E.,
721 Finney, S.C., Sheets, H.D., 2009. Local and global perspectives on carbon and
722 nitrogen cycling during the Hirnantian glaciation. Palaeogeogr. Palaeoclimatol.
723 Palaeoecol. 276, 182–195.
724 Lenton, T.M., Crouch, M., Johnson, M., Pires, N., Dolan, L., 2012. First plants cooled the
725 Ordovician. Nat. Geosci. 5, 86–89.
726 Li, C., Zhang, J., Li, W., Botting, J., Chen, Q., Fan, J., Zhang, Y., 2021. Multiple
727 glacio-eustatic cycles and associated environmental changes through the
728 Hirnantian (Late Ordovician) in South China. Glob. Planet. Change 207, 103668.
729 Li, M., Lei, Y., Feng, L., Wang, Z., Belshaw, N.S., Hu, Z., Liu, Y., Zhou, L., Chen, H., Chai, X.,
730 2018. High-precision Ca isotopic measurement using a large geometry high
731 resolution MC-ICP-MS with a dummy bucket. J. Anal. At. Spectrom. 33, 1707–

1719.

Li, W., 2021, Darriwilian to Katian (Ordovician) depositional characteristics and their implications for geological events in South China. University of Chinese Academy of Sciences (Ph.D. thesis), Beijing, 187 p.

Liang, Y., Liu, Z.R., Algeo, T.J., Meng, L., Ming, C., Wang, J., Song, B., Liu, Z., Zhou, M.-F., 2024. Contrasting dynamics of marine bacterial-algal communities between the two main pulses of the Late Ordovician Mass Extinction. Earth Planet. Sci. Lett. 645, 118956.

Lin, S., Wang, L., Xiao, W., Xing, G., Niu, Z., Zhao, X., Yin, C., Zhang, S., Liu, H., 2024. The early Paleozoic Wuyi–Yunkai orogeny in South China: a collisional orogeny with a major lag in time between onset of collision and peak metamorphism in subducted continental crust. Geol. Soc. Lond. Spec. Publ. 542, SP542-2023-2026.

Longman, J., Mills, B.J.W., Manners, H.R., Gernon, T.M., Palmer, M.R., 2021. Late Ordovician climate change and extinctions driven by elevated volcanic nutrient supply. Nat. Geosci. 14, 924-929.

Luo, Q., Goodarzi, F., Zhong, N., Qiu, N., Wang, X., Suchý, V., Khan, I., Zheng, X., Liu, B., Ardakani, O.H., Zhang, Y., Li, D., Wu, J., Fang, Z., Shi, R., Skovsted, C.B., Sanei, H., Xu, Y., Wu, J., Hu, W., Duan, G., 2025. Dispersed organic matter from pre-Devonian marine shales: A review on its composition, origin, evolution, and potential for hydrocarbon prospecting. Earth Sci. Rev. 261, 105027.

Melchin, M.J., Holmden, C., 2006. Carbon isotope chemostratigraphy in Arctic Canada:

753 Sea-level forcing of carbonate platform weathering and implications for Hirnantian
754 global correlation. Palaeogeogr. Palaeoclimatol. Palaeoecol. 234, 186–200.
755 Meyers, P.A., 1994. Preservation of elemental and isotopic source identification of
756 sedimentary organic matter. Chem. Geol. 114, 289–302.
757 Oehlert, A.M., Swart, P.K., 2014. Interpreting carbonate and organic carbon isotope
758 covariance in the sedimentary record. Nat. Commun. 5, 4672.
759 Panchuk, K.M., Holmden, C., Kump, L.R., 2005. Sensitivity of the epeiric sea carbon
760 isotope record to local-scale carbon cycle processes: Tales from the Mohawkian
761 Sea. Palaeogeogr. Palaeoclimatol. Palaeoecol. 228, 320–337.
762 Patterson, W.P., Walter, L.M., 1994. Depletion of 13C in seawater ΣCO_2 on modern
763 carbonate platforms: Significance for the carbon isotopic record of carbonates.
764 Geology 22, 885–888.
765 Pohl, A., Donnadieu, Y., Le Hir, G., Ladant, J.-B., Dumas, C., Alvarez-Solas, J.,
766 Vandenbroucke, T.R.A., 2016. Glacial onset predated Late Ordovician climate
767 cooling. Paleoceanography 31, 800–821.
768 Popp, B.N., Laws, E.A., Bidigare, R.R., Dore, J.E., Hanson, K.L., Wakeham, S.G., 1998.
769 Effect of Phytoplankton Cell Geometry on Carbon Isotopic Fractionation. Geochim.
770 Cosmochim. Acta 62, 69–77.
771 Qiu, Z., Liu, B., Lu, B., Shi, Z., Li, Z., 2022a. Mineralogical and petrographic
772 characteristics of the Ordovician-Silurian Wufeng-Longmaxi Shale in the Sichuan
773 Basin and implications for depositional conditions and diagenesis of black shales.

Mar. Pet. Geol. 135, 105428.

Qiu, Z., Zou, C., Mills, B.J.W., Xiong, Y., Tao, H., Lu, B., Liu, H., Xiao, W., Poulton, S.W., 2022b. A nutrient control on expanded anoxia and global cooling during the Late Ordovician mass extinction. Commun. Earth Environ. 3, 1–9.

Qiu, Z., Zou, C., 2020. Controlling factors on the formation and distribution of "sweet-spot areas" of marine gas shales in South China and a preliminary discussion on unconventional petroleum sedimentology. J. Asian Earth Sci. 194, 103989.

Romanek, C.S., Grossman, E.L., Morse, J.W., 1992. Carbon isotopic fractionation in synthetic aragonite and calcite: Effects of temperature and precipitation rate. Geochim. Cosmochim. Acta 56, 419–430.

Rong, J., Harper, D.A.T., Huang, B., Li, R., Zhang, X., Chen, D., 2020. The latest Ordovician Hirnantian brachiopod faunas: New global insights. Earth Sci. Rev. 208, 103280.

Sánchez-Roda, A., Wignall, P.B., Xiong, Y., Poulton, S.W., 2024. Redox changes in the Iapetus Ocean during the Late Ordovician extinction crises. J. Geol. Soc. London 181, jgs2023-2195.

Tang, J., Köhler, S.J., Dietzel, M., 2008. Sr^{2+}/Ca^{2+} and $^{44}Ca/^{40}Ca$ fractionation during inorganic calcite formation: I. Sr incorporation. Geochim. Cosmochim. Acta 72, 3718–3732.

Torsvik, T.H., Cocks, L.R.M., 2013. Gondwana from top to base in space and time.

795 Gondwana Res. 24, 999–1030.

796 Wang, Y., Qiu, N., Borjigin, T., Shen, B., Xie, X., Ma, Z., Lu, C., Yang, Y., Yang, L., Cheng, L.,

797 Fang, G., Cui, Y., 2019. Integrated assessment of thermal maturity of the Upper

798 Ordovician–Lower Silurian Wufeng–Longmaxi shale in Sichuan Basin, China. Mar.

799 Pet. Geol. 100, 447–465.

800 Watanabe, Y., Naraoka, H., Wronkiewicz, D.J., Condie, K.C., Ohmoto, H., 1997. Carbon,

801 nitrogen, and sulfur geochemistry of Archean and Proterozoic shales from the

802 Kaapvaal Craton, South Africa. Geochim. Cosmochim. Acta 61, 3441–3459.

803 Wu, J., Liang, C., Yang, R.-C., Hu, Z., Li, W., Xie, J., 2022. The genetic relationship

804 between paleoenvironment, mineral compositions and lithofacies in the

805 Ordovician–Silurian Wufeng–Longmaxi sedimentary succession in the Sichuan

806 Basin, SW China. J. Asian Earth Sci. 236, 105334.

807 Yan, D., Chen, D., Wang, Q., Wang, J., 2012. Predominance of stratified anoxic Yangtze

808 Sea interrupted by short-term oxygenation during the Ordo-Silurian transition.

809 Chem. Geol. 291, 69-78.

810 Yang, S., Fan, J., 2025. Decreased marine organic carbon burial during the Hirnantian

811 glaciation. Earth Planet. Sci. Lett. 654, 119240.

812 Yang, S., Fan, J., Algeo, T.J., Shields, G.A., Zhou, Y., Li, C., Chen, J., Li, W., Li, N., Cao, J.,

813 Zhang, L., Sun, Z., Shen, S., 2024. Steep oceanic DIC $\delta^{13}C$ depth gradient during the

814 Hirnantian Glaciation. Earth Sci. Rev. 255, 104840.

815 Zhang, J., Li, C., Zhong, Y., Wu, X., Fang, X., Liu, M., Chen, D., Gill, B.C., Algeo, T.J., Lyons,

T.W., Zhang, Y., Tian, H., 2024. Linking carbon cycle perturbations to the Late Ordovician glaciation and mass extinction: A modeling approach. Earth Planet. Sci. Lett. 631, 118635.

Zhong, Y., Wu, H., Fan, J., Fang, Q., Shi, M., Zhang, S., Yang, T., Li, H., Cao, L., 2020. Late Ordovician obliquity-forced glacio-eustasy recorded in the Yangtze Block, South China. Palaeogeogr. Palaeoclimatol. Palaeoecol. 540, 109520.

Zou, C., Qiu, Z., Poulton, S.W., Dong, D., Wang, H., Chen, D., Lu, B., Shi, Z., Tao, H., 2018. Ocean euxinia and climate change “double whammy” drove the Late Ordovician mass extinction. Geology 46, 535–538.

826 **Table 1** Parameters in the early marine diagenesis model.

Parameter	Description	Value	Reference
α_{Ca}	Ca isotopic fractionation factor for diagenesis	1.000	
α_C	C isotopic fractionation factor for diagenesis	1.001	
φ	Porosity	0.5	
ρ_s	Density of sediment (g/cm^3)	1.8	
ρ_f	Density of fluid (g/cm^3)	1.0125	Ahm et al., 2018
R	Reaction rate (%/myr)	10	
u	Advection rate (m/yr)	0.1	
M_s	Mass of element in primary sediment (%)	C = 12 Ca = 39	
M_f	Mass of element in fluid (mol/kg)	C = 0.01028 Ca = 0.002	
δ_s	Isotopic composition of primary sediments (‰)	$\delta^{13}C$ = 2 $\delta^{44}Ca$ = -2	This study
δ_f	Isotopic composition of initial fluid (‰)	$\delta^{13}C$ = -3.4 $\delta^{44}Ca$ = -0.5	Holmden et al., 2024

827

Figure captions

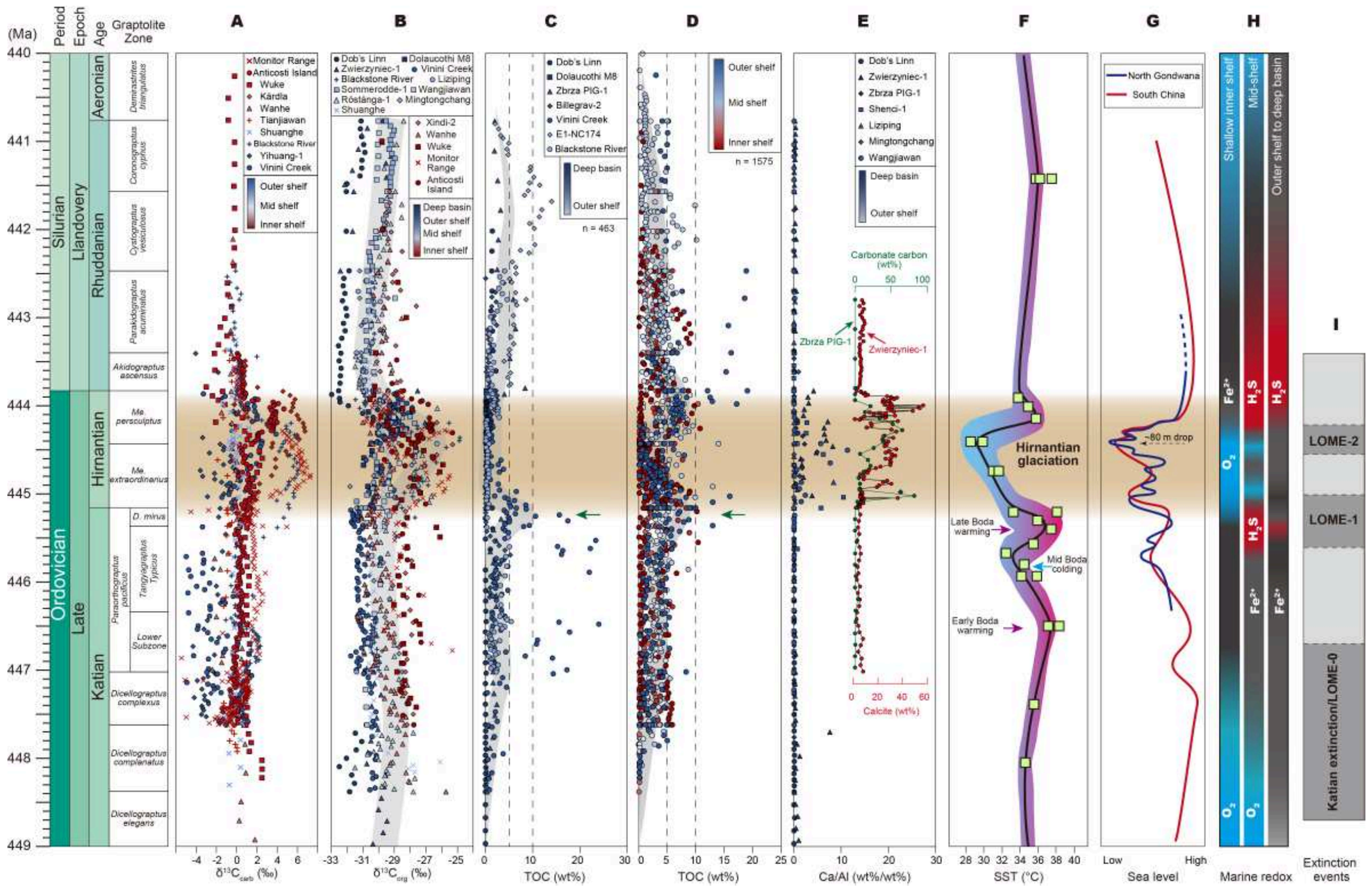

Fig. 1. Compilation of geochemical data, environmental context and biological extinction. (A) Compilation of global $\delta^{13}C_{carb}$ records. (B) Global $\delta^{13}C_{org}$ records. (C) Total organic carbon (TOC) records for deep marine settings. (D) TOC records for the Yangtze Shelf. (E) Ca enrichment in deep marine settings. (F) Tropical sea-surface temperature (SST) reconstruction (Finnegan et al., 2011). (G) Sea-level history in the high-paleolatitude North Gondwana (Ghienne et al., 2014) and the low-paleolatitude South China. (H) Marine redox reconstruction based on iron speciation and redox-sensitive element proxies. Inner to mid-shelf conditions are inferred from the Yangtze Shelf, South China (Zou et al., 2018), whereas outer shelf to basin conditions from the deep-marine Dob's Linn section, UK (Dahl et al., 2021; Sánchez-Roda et al.,

2024). (I) Black-grey zoned boxes represent three intervals of the Late Ordovician mass extinction (LOME) (Deng et al., 2021). See Supplementary Materials for data sources, section locations and full references. *Me.*, *Metabolograptus*; *D.*, *Dicerarograptus*.

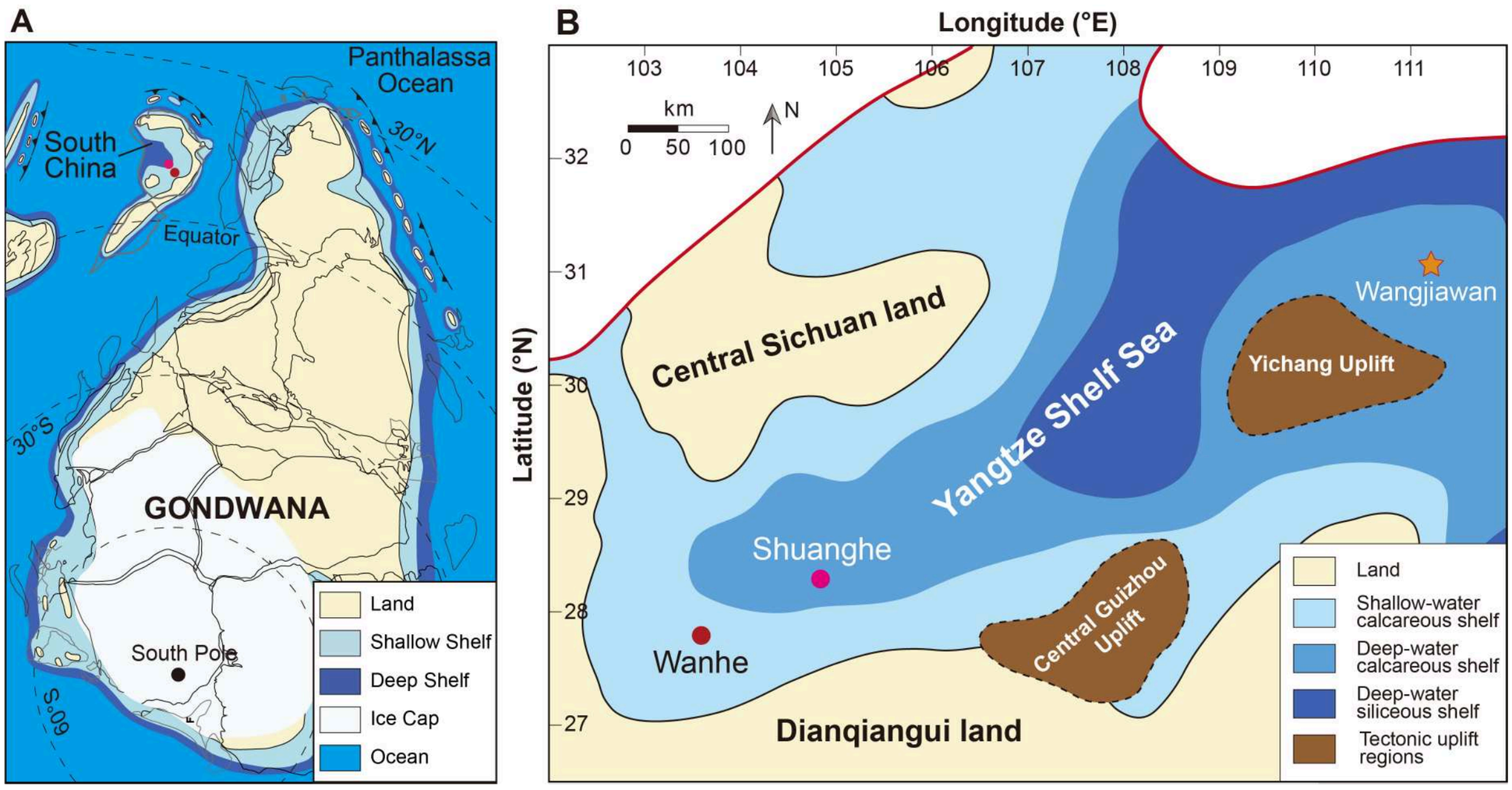

Fig. 2. Paleogeographic characteristics. (A) Location of South China relative to the Gondwana supercontinent in the latest Ordovician (~445 Ma) (Torsvik and Cocks, 2013). (B) Locations of sampled sections on the Yangtze Shelf (Qiu and Zou, 2020). The extent of the Central Guizhou and Yichang uplifts is redrawn from Chen et al. (2001) and (2018). Red lines indicate boundary faults separating tectonic plates.

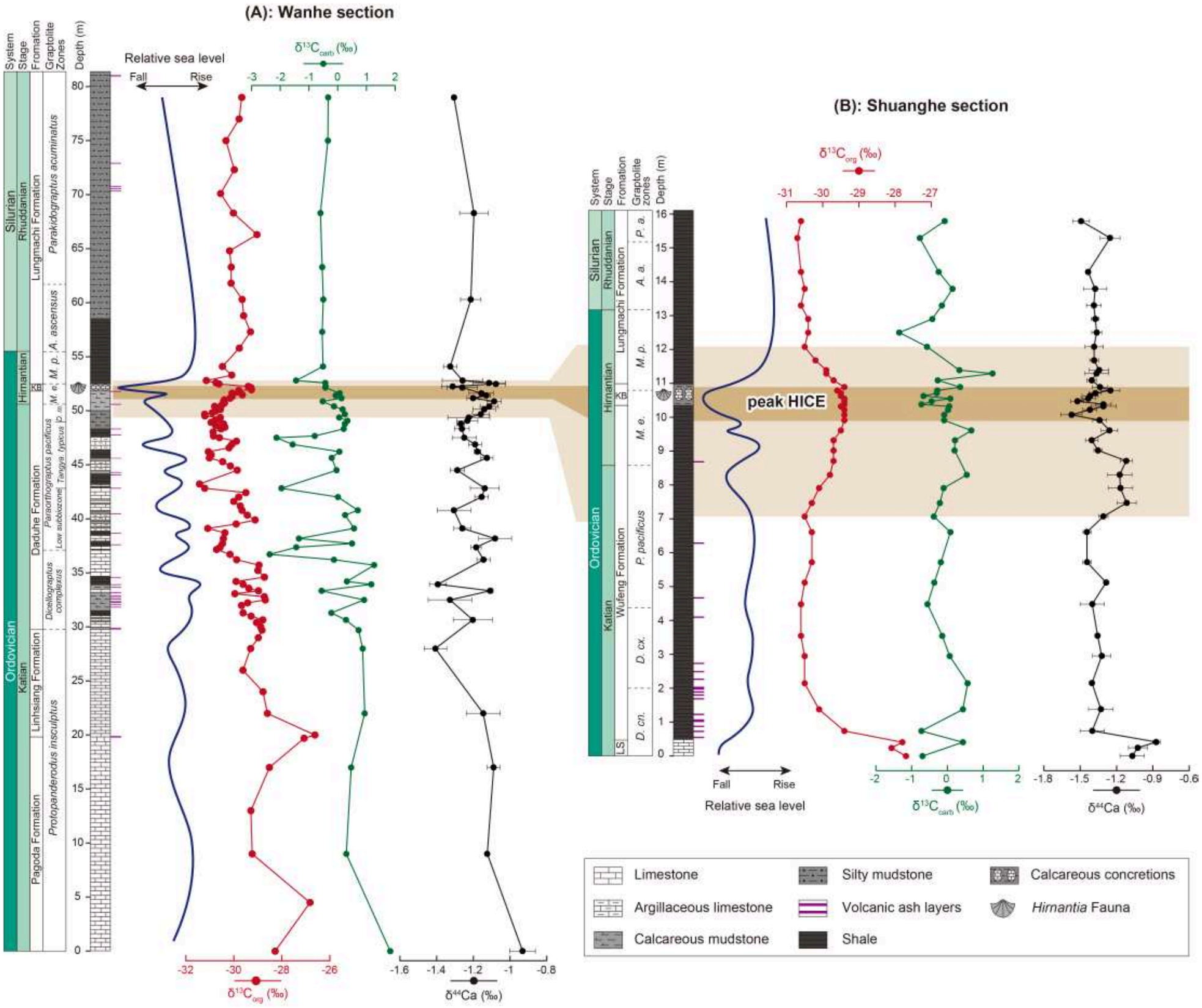

Fig. 3. Integrated geochemical records for the Wanhe and Shuanghe sections. The light-brown shaded band denotes the HICE interval, and the brown shaded region represents the peak HICE interval. The graptolite zones of the Wanhe section are from Li (2021), and those of the Shuanghe section are from Zou et al. (2018). $\delta^{13}C_{org}$ data for the Shuanghe section are from Zou et al. (2018). Error bars on $\delta^{44}Ca$ data represent 2σ uncertainty. LS, Linhsiang; KB, Kuanyinchiao Bed. Full names of graptolite zones are provided in Fig. 1.

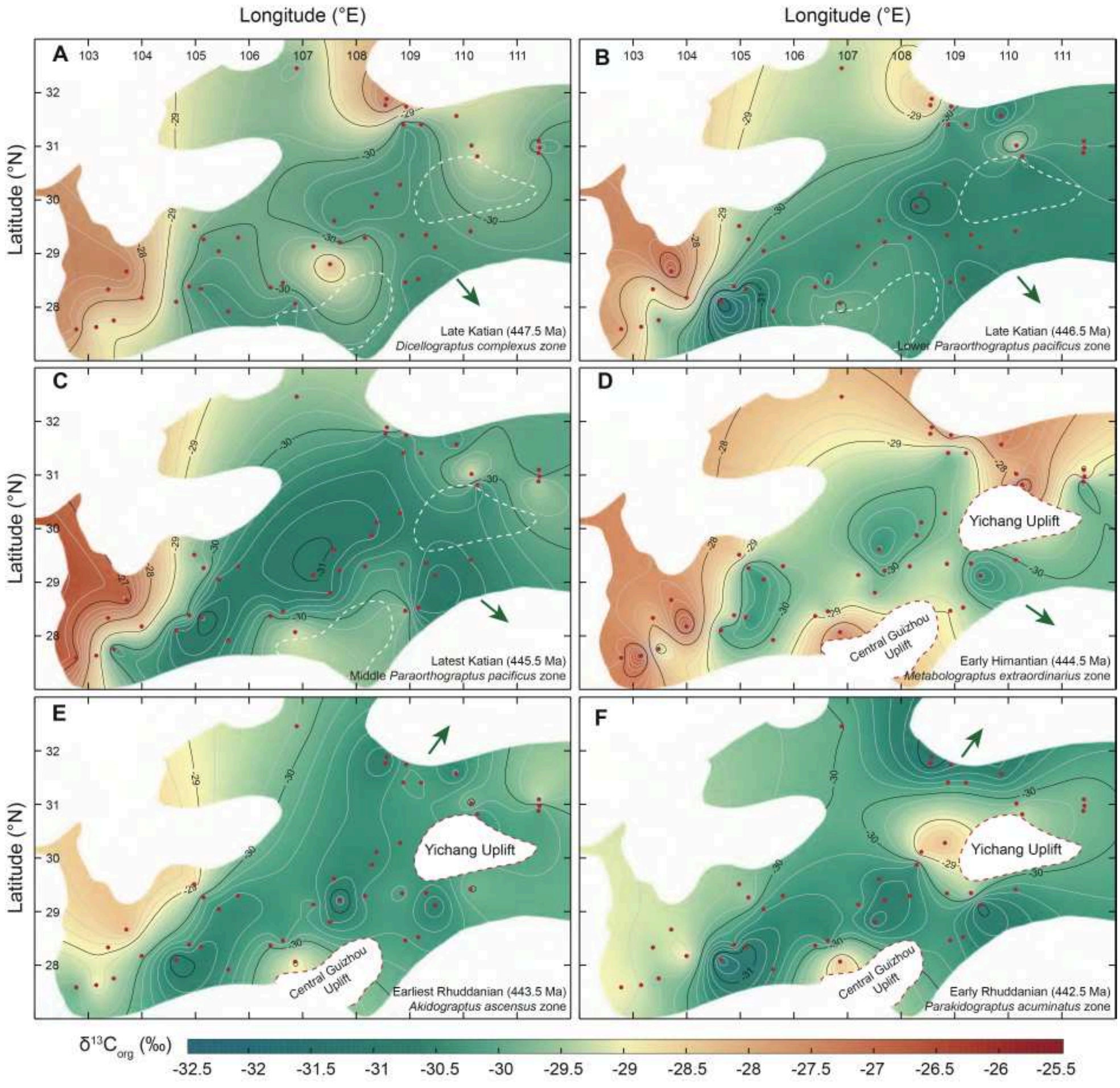

860

861 **Fig. 4.** Individual maps showing spatial variability in $\delta^{13}C_{org}$ values on the Yangtze

862 Shelf across the Hirnantian glaciation. No sedimentary records in the white areas. The

863 white dotted line indicates the extent of the submarine highs. Red dots illustrate the

864 distribution of all sections and cores (see Fig. S2 and Table S3 for present-day

865 locations and data sources). Green arrows indicate directions toward the deep slope

866 and open ocean.

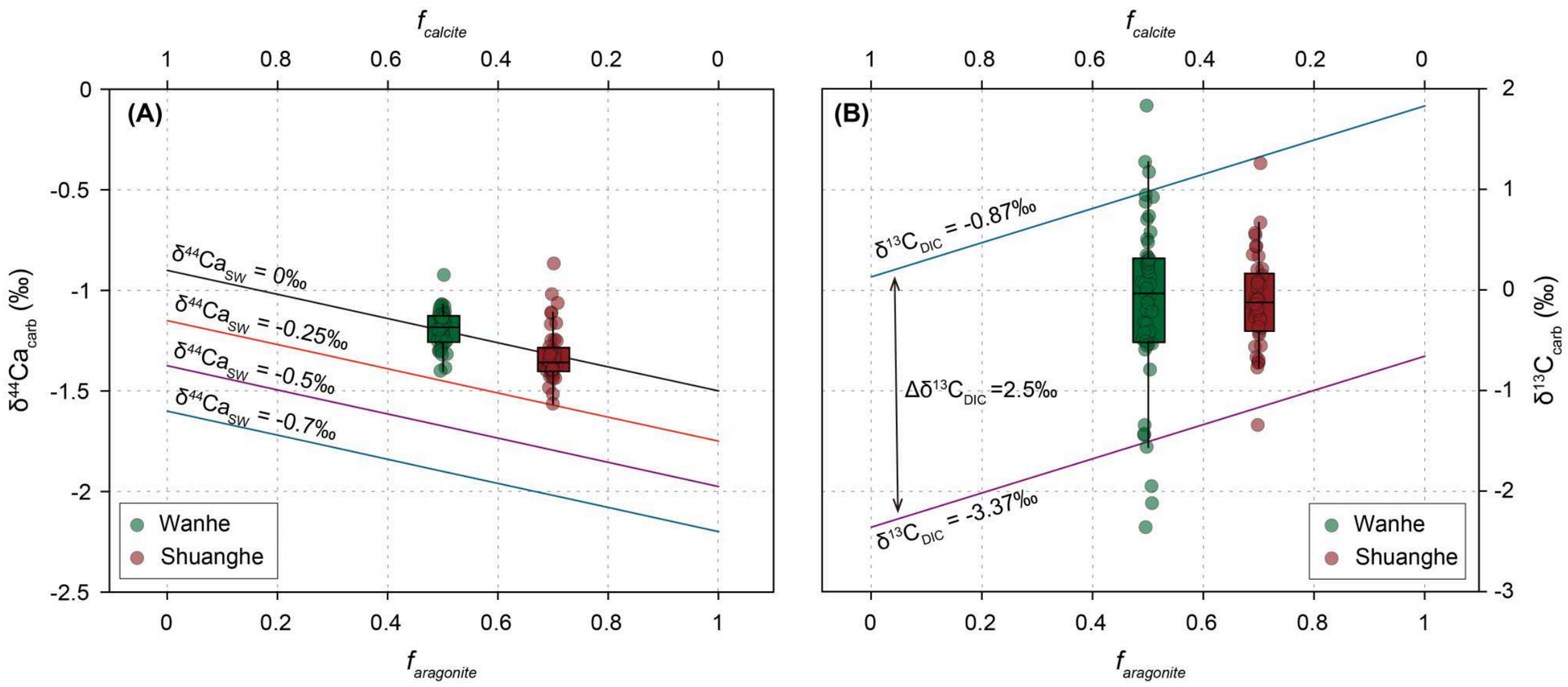

867

868 **Fig. 5.** Two-endmember mixing model of aragonite and calcite (Adiatma et al., 2024),
869 and the range of measured $\delta^{44}Ca$ and $\delta^{13}C_{carb}$ data points from the Wanhe and
870 Shuanghe sections. The positions of the $\delta^{44}Ca$ and $\delta^{13}C_{carb}$ data points on the *x*-axis
871 are determined by the estimated fraction of aragonite ($f_{aragonite}$), based on the mean
872 $\delta^{44}Ca$ values. In the $\delta^{44}Ca$ model (A), four aragonite-calcite mixing lines represent
873 variable seawater $\delta^{44}Ca$ values, ranging from -0.7‰ to -0.25‰ for the
874 Ordovician-Silurian ocean (~-0.5‰ for normal marine seawater), and ~0‰ for the
875 modern ocean (Gussone et al., 2020; Holmden et al., 2024). In the $\delta^{13}C_{carb}$ model (B),
876 two aragonite-calcite mixing lines illustrate that reproducing measured $\delta^{13}C_{carb}$ values
877 requires a ~2.5‰ variability in seawater $\delta^{13}C_{DIC}$ (i.e., $\Delta\delta^{13}C_{DIC}$). No single theoretical
878 mixing line can account for all measured data points, suggesting that changes in
879 carbonate mineralogy alone cannot fully explain the observed $\delta^{44}Ca$ and $\delta^{13}C_{carb}$
880 trends in our sections.

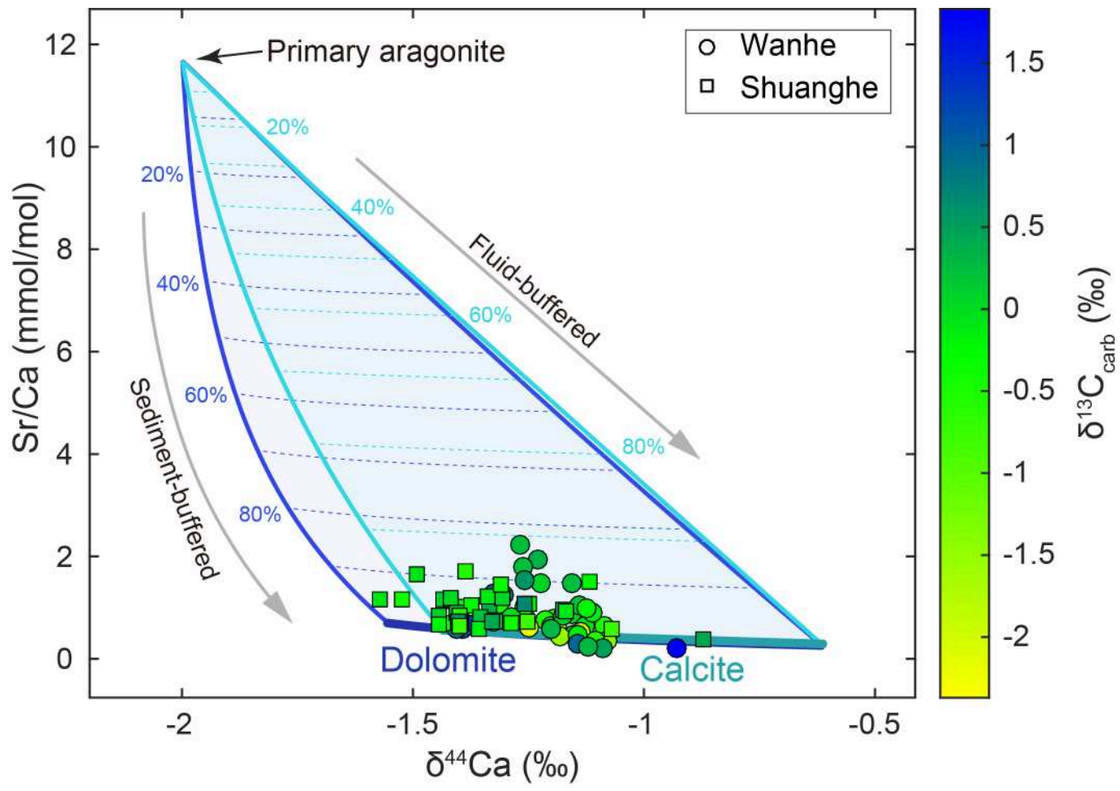

Fig. 6. Modeled trajectories showing the correlation between Sr/Ca ratios and $\delta^{44}Ca$ in the bulk sediment during neomorphism (light cyan field) and dolomitization (light purple field), compared with measured data from the Shuanghe and Wanhe sections. The fill color of the symbols indicates $\delta^{13}C_{carb}$ values. Dashed lines within the diagenetic envelopes indicate the degree of diagenesis from 0% to 100%. Thick lines represent the fully diagenetic minerals, calcite and dolomite.

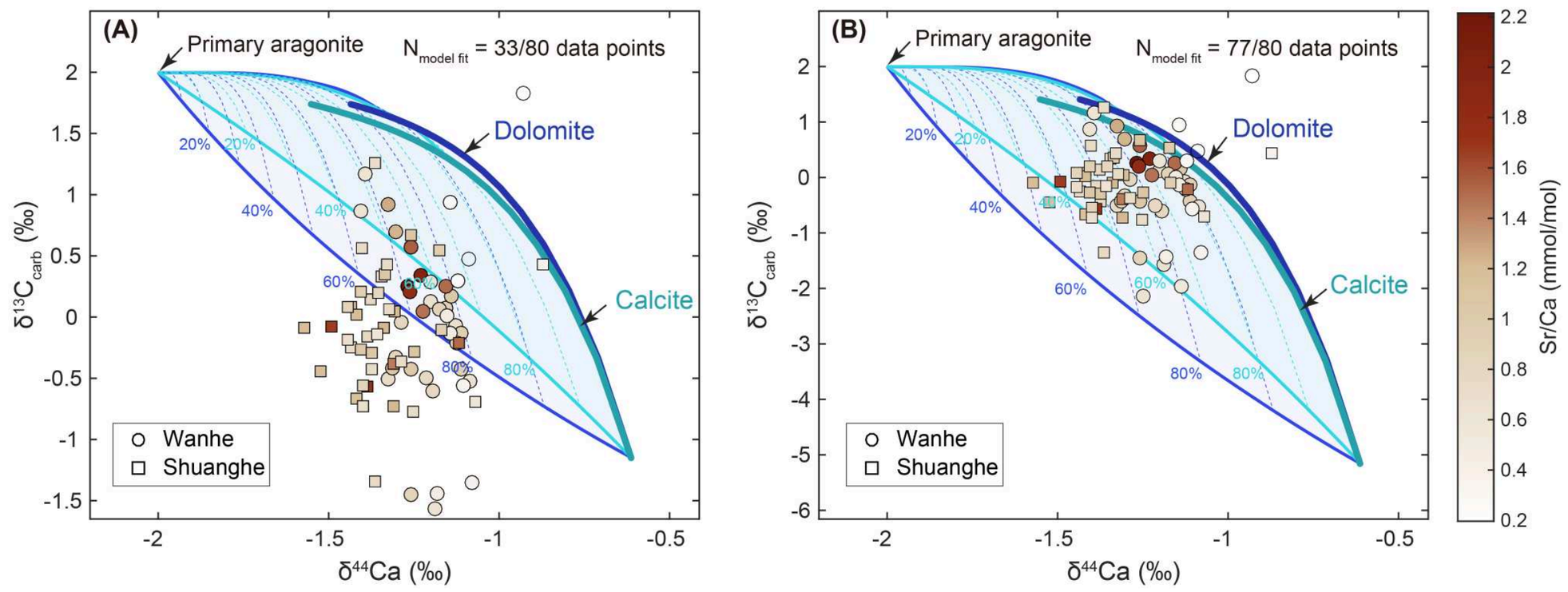

Fig. 7. Modeling results of the diagenetic transformation from aragonite to calcite (neomorphism, light cyan field) or dolomite (dolomitization, light purple field),

compared with measured data from the Shuanghe and Wanhe sections. In modeling Scenario A, the $\delta^{13}C$ value of the initial diagenetic fluid is set to -3.4‰, representing our best estimate of diagenetic conditions based on the lightest $\delta^{13}C_{carb}$ value of -2.37‰ in our data. In Scenario B, the $\delta^{13}C$ value is set to -9‰ to broaden the model fit to the measured data, although this value may be less realistic for Ordovician–Silurian diagenetic environments. The fill color of the symbols indicates carbonate Sr/Ca ratios.

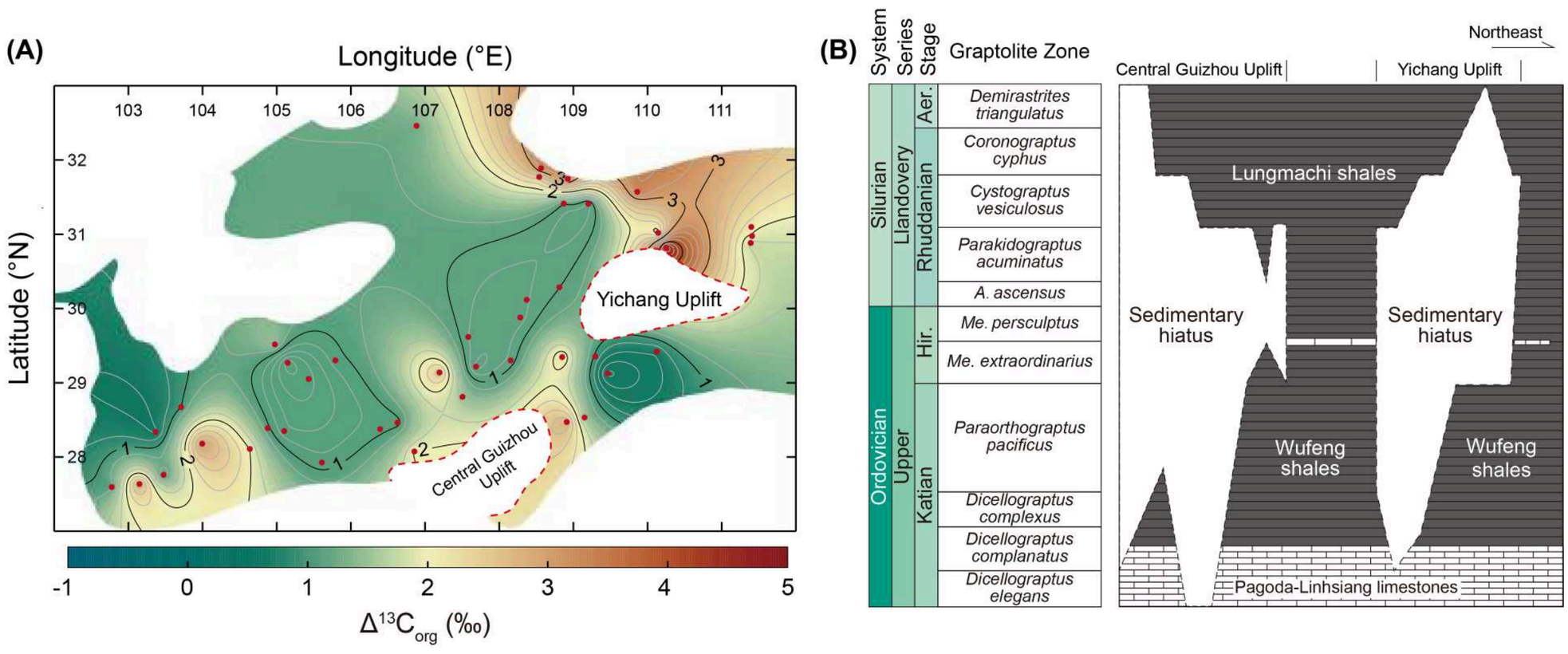

Fig. 8. Spatial variability in HICE amplitude ($\Delta^{13}C_{org}$) across the Yangtze Shelf (A), and the Late Ordovician– early Silurian stratigraphic succession from Central Guizhou to Yichang show a sedimentary hiatus between Late Ordovician limestones and early Silurian shales (B) (Chen et al., 2001). Full names of graptolite zones are provided in Fig. 1. Hir., Hirnantian; Aer., Aeronian.